Defect redistribution along grain boundaries in SrTiO$_3$ by externally applied electric fields

Boyi Qu [a], Daria Eiteneer [a], Lauren A. Hughes [a], Jan-Helmut Preusker [b], Joseph Wood [a], Wolfgang Rheinheimer [c], Michael J. Hoffmann [b], Klaus van Benthem [a,*]

[a] Department for Materials Science and Engineering, University of California, Davis, Davis, CA 95616, USA
[b] Institute for Applied Materials - Ceramic Materials and Technologies, Karlsruhe Institute of Technology, Haid-und-Neu-Strasse 7, 76131 Karlsruhe, Germany
[c] Forschungszentrum Jülich GmbH, Wilhelm-Johnen-Straße, 52428 Jülich, Germany

ARTICLE INFO

ABSTRACT

During thermal annealing at 1425 °C nominal electric field strengths of 50 V/mm and 150 V/mm were applied along the grain boundary planes of a near 45° (100) twist grain boundary in SrTiO$_3$. Electron microscopy characterization revealed interface expansions near the positive electrode around 0.8 nm for either field strength. While the interface width decreased to roughly 0.4 nm after annealing at 50 V/mm, the higher field strength caused decomposition of the boundary structure close to the negative electrode. Electron energy-loss and X-ray photoelectron spectroscopies demonstrated an increased degree of oxygen sublattice distortion at the negative electrode side, and enhanced concentrations of Ti^{3+} and Ti^{2+} compared to bulk for both single crystals and bicrystals annealed with an external electric field, respectively. Oxygen migration due to the applied electric field causes the observed alteration of grain boundary structures. At sufficiently high field strength the agglomeration of anion vacancies may lead to the decomposition of the grain boundary.

1. Introduction

The effect of electric fields on the sintering of ceramic powder compacts has been studied extensively in the past [1]. Field assisted sintering, spark plasma sintering (SPS) and flash sintering all utilize applied electric fields and resulting currents to enhance densification [2–6]. In addition, externally applied electric fields can decrease the required sintering temperatures or applied pressures, and can enhance or suppress grain growth [2,7–13]. Qin and co-workers discovered electrode effects on microstructure development of yttrium-stabilized zirconia during flash sintering with an applied DC bias [14]. Enhanced grain growth was observed near the cathode, which is attributed to the DC bias lowering the activation energy for cation migration owing to local reduction-oxidation reactions [14]. Jeong and co-workers observed an increased grain boundary migration rate in Al$_2$O$_3$ when an external electric field was applied during sintering [15]. Mishra and co-workers reported blackening behavior of polycrystalline gadolinium-doped ceria during flash sintering, indicating the migration of oxygen vacancies towards the cathode [1,16].

From this brief literature survey, it becomes evident that there must be a strong interaction of grain boundaries in the evolving microstructure and externally applied electric fields. In a model study by Hughes et al. [18,19] an electric field was directed perpendicularly across the grain boundary plane during diffusion bonding of a 42° (100) twist grain boundaries in SrTiO$_3$. In the absence of any externally applied electric field, diffusion bonding resulted in a width of the grain boundary core of around 0.8 nm. However, the interface expansion was only approximately 0.4 nm after diffusion bonding in the presence of an externally applied electric field. It was hypothesized that the oppositely charged (100) interface planes of the two half crystals formed a large oxygen vacancy concentration gradient across the forming boundary plane and resulted in the smaller width of the grain boundary core [18,19]. Electron energy loss spectroscopy further revealed disordering on the oxygen sublattice for increasing applied field strengths. Hughes et al. have further shown that the observed grain boundary core modifications accomplished by electric fields during diffusion bonding were only meta-stable and relied on surface modifications by the electric field prior to the joining process [19].

While previous studies about the alteration of grain boundary core structures by externally applied electric fields have mostly considered

---

electric field directions perpendicular to the interface plane. Grain boundaries in a polycrystalline microstructure can occur at any angle with respect to the direction of the electric field. For this more general case Rheinheimer and co-workers have suggested electric field induced defect redistribution in strontium titanate [13,17]. The hypothesis for this study was electric field induced oxygen vacancy migration along the grain boundary cores in SrTiO$_3$. Structural transformations of near 45° (100) twist grain boundaries were discovered after annealing of bicrystals in the presence of electric fields directed along the grain boundary plane. A variety of experimental techniques, including high angle annular dark field STEM (HAADF-STEM), electron energy loss spectroscopy (EELS) and X-ray photoelectron spectroscopy (XPS) were used to characterize atomic and electronic grain boundary structures as a function of relative distance to the electrodes employed for applying electric fields parallel to the grain boundary plane. Comparison of the SrTiO$_3$ grain boundary core structures near the positive and negative electrodes for two different electric field strengths provides evidence for oxygen vacancy re-distribution and potential decomposition.

2. Experimental techniques

Single crystals of SrTiO$_3$ (SurfaceNet GmbH, Rheine, Germany) were diffusion bonded at 1425 °C under a uniaxial pressure of 1 MPa to form near 45° (100) twist grain boundaries. Application of moderate pressures below 6 MPa for SrTiO$_3$ [18,20,21] enhances interfacial bonding via deformation of asperities, minimizing pore sizes, and increasing dislocation densities which promotes cation diffusion [22–24]. After diffusion bonding completed, the bicrystals were annealed at 1425 °C for 1 h while an electrostatic field was applied in the direction along the grain boundary plane. Fig. 1 presents a sketch of the experimental setup. For the application of the electric field, two parallel Pt-Rh electrodes were used that were electrically isolated from the bicrystal by roughly 1 mm thick aluminum oxide layers. To avoid solid-state reactions between SrTiO$_3$ and Al$_2$O$_3$, a thin layer of zirconia powder (grade GL10, Luxfer Mel Technologies) separating the bicrystal from the Al$_2$O$_3$ layers was added. The layer of zirconia also enabled easier separation of the different ceramic materials after thermal annealing.

Annealing experiments were carried out with biases U applied to the electrodes that were separated from each other by a distance d. Based on the experimental geometry (cf. Fig. 1), the two resulting applied nominal electric field strengths were $U_{low}/d = 50$ V/mm and $U_{high}/d = 150$ V/mm. The electric field across the SrTiO$_3$ bicrystal is smaller than the externally applied nominal field E_{total} due to the relatively low

dielectric constant of aluminum oxide. In accordance with earlier work by Rheinheimer and co-workers [13,17] the electric field across SrTiO$_3$ (E_{STO}) was calculated using Eq. 1 under the assumption that the SrTiO$_3$ crystals and the alumina layers can be represented by a series of capacitors with different dielectric constant.

$$\frac{E_{STO}}{E_{total}} = \frac{d_{STO} + d_i}{d_{STO}\left(1 + \frac{\varepsilon_{r,\,STO}d_i}{\varepsilon_{r,\,alumina}d_{STO}}\right)} \tag{1}$$

d_{STO} is the dimension of the SrTiO$_3$ bicrystal in the direction of the applied field, i.e., the length of the grain boundary plane, d_I is the thickness of the alumina layer, $\varepsilon_{r,\,STO}$ and $\varepsilon_{r,\,alumina}$ are the dielectric constant of SrTiO$_3$ and alumina, respectively. The layer of zirconia powder further reduces the effective field strength across the SrTiO$_3$ to $E_{STO,low} = 26.4$ V/mm and $E_{STO,high} = 79.3$ V/mm, respectively [13].

After thermal annealing in the presence of an electric field, which will be referred to as *electric field annealing* throughout the remainder of this publication, the structural homogeneity of the bicrystals was qualitatively assessed by scanning electron microscopy. Secondary electron (SE) imaging of the areas that include the grain boundary over the full length of the grain boundary plane was carried out using either a FEI Scios dual-beam focused ion beam (FIB) instrument (FEI, Hillsboro, OR), or a Thermo Fischer Quattro environmental scanning electron microscope (Thermo Fisher Scientific, Hillsboro, OR). The Thermo Fisher MAPS3.2 software was used to automatically capture between 612 and 765 individual high magnification SE micrographs and subsequently splice them together by maximizing cross-correlation functions in overlapping areas. This process generates large field-of-view electron micrographs with potential topography contrast indicating grain boundary grooving. Secondary electron imaging was previously successfully employed to assess the quality of interfacial bonding of SrTiO$_3$ bicrystals fabricated by SPS [25,26].

Grain boundaries were prepared for cross-sectional transmission electron microscopy (TEM) characterization using FIB sectioning. Electron transparent lamellae were extracted for each bicrystal from areas close to the positive and negative electrode, respectively. After thinning lamellae to around 200 nm and 300 nm using the FIB instrument, a Fischione Nanomill instrument (Fischione Industries, Export, PA) was employed to reduce TEM sample thicknesses to around 50 nm using a low-energy Ar$^+$ ion beam.

Atomic grain boundary structures were characterized by aberration-corrected HAADF-STEM imaging. Samples of the bicrystal annealed at 50 V/mm were imaged with a JEOL JEM 2100AC aberration-corrected STEM installed at UC Davis and operated at 200 kV. The bicrystal annealed in the presence of a nominal electric field strength of 150 V/mm was characterized with an acceleration voltage of 300 kV utilizing the FEI TEAM 0.5 instrument installed at Lawrence Berkeley National Laboratory. The local electronic grain boundary core structures were determined by spatially resolved EELS. Spectra of the O K and Ti L$_{2,3}$ absorption edges were recorded with a Gatan Imaging Filter (GIF Tridem; Gatan Inc. Pleasanton, CA) attached to the JEOL JEM 2100AC microscope. The energy dispersion during EELS acquisition was 0.1 eV/channel and pixel dwell times were either 0.1 or 0.2 s/spectrum. The probe-forming convergence semi-angle and the collection semi-angle were both 16 mrad. All acquired spectra were background subtracted using a power-law fitting procedure [27]. Principle component analysis (PCA) was applied to all background subtracted spectra to improve signal-to-noise ratios using the singular value decomposition algorithm in HyperSpy [28]. The near-edge fine structures (ELNES) of the background subtracted Ti L$_{2,3}$ edge spectra were reconstructed from the first 8 components of the PCA deconstruction. The O K ELNES were reconstructed from the first 6 components. All ELNES plots were calibrated with respect to the edge onset of the bulk spectrum, i.e., the energy-loss at which the second derivative of the bulk spectrum equals zero. Energy dispersive X-ray spectroscopy (EDXS) line profiles were recorded across the grain boundaries with an Oxford Aztec Energy TEM Advanced
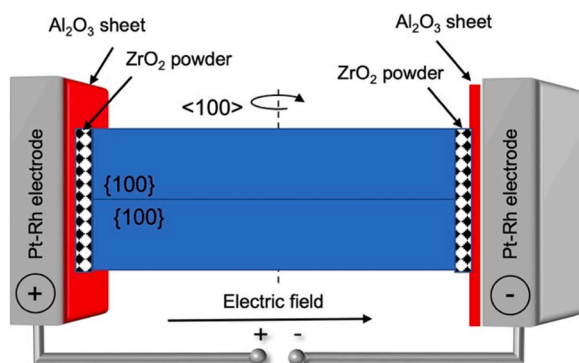

Fig. 1. Sketch of the experimental setup for thermal annealing of bicrystals during simultaneous application of electric fields. The two half single crystals are represented by the blue blocks. The upper crystal is rotated by nominally 45° around a common <100> axis to form a (100) twist boundary. Electric bias was applied to parallel Pt-Rh electrodes. The bicrystal was cut and polished on the sides facing the electrodes. 1 mm thick Al$_2$O$_3$ sheets were used to electrically isolate the electrodes from the SrTiO$_3$ crystals. Thin layers of ZrO$_2$ powder were used to minimize solid state reactions between SrTiO$_3$ and Al$_2$O$_3$.

Microanalysis System with an X-MaxN TSR Windowless large area Analytical Silicon Drift Detector.

X-ray photoelectron spectroscopy (XPS) measurements of Ti 2p signals were carried out using a Kratos AXIS Supra instrument equipped with a monochromatic Al K_α source ($h\nu = 1486.6$ eV). XPS data were acquired at 150 W (10 mA, 15 kV) from surfaces of the bicrystals that faced the negative electrode during electric field annealing. A slot aperture was employed with an energy resolution of about 1.6 eV, a dwell time of 600 ms, and a step size of 0.040 eV. Single crystals of $SrTiO_3$ were field annealed using the same temperature (1425 °C) and field strength as the bicrystals. XPS data from the single crystals were acquired in cross-section from 4 or 5 equidistant locations between the electrodes. Spectra were recorded using a 55 μm circular aperture with a dwell time of 200 ms and a step size of 0.015 eV. The Kratos ESCApe software was used for data acquisition and subsequent peak area fitting. Intensity minima were identified on both sides of the Ti 2p peak doublet and a Shirley [29] background was fitted to the corresponding energy interval. Each spectrum was subsequently fitted with six asymmetrical Gaussian-Lorentzian peaks. Details of the fitting procedure are included in the Supplementary Materials. For direct comparison, individual XPS spectra were background-subtracted. The largest spectral intensity, i.e., the maximum of the main Ti 2p peak in bulk $SrTiO_3$ was calibrated to an energy of 458.4 eV.

3. Results

3.1. SEM imaging

Fig. 2 displays large field of view SEM maps of the bicrystals after field annealing. For Fig. 2(a) the location of the grain boundary plane after field annealing at 50 V/mm was ascertained from high resolution micrographs recorded from the edges of the bicrystal close to the two electrodes and is indicated by a dashed line. No SE contrast resulting from grain boundary grooving can be observed. Fig. 2(b) and (c) show enlarged SEM maps recorded form the bicrystal close to the positive and negative electrode, respectively. Fig. 2(d) shows a low magnification

SEM map of the bicrystal after field annealing at 150 V/mm. Close to the positive electrode (cf. Fig. 2(e)) no topography contrast due to grain boundary grooving was detected, while close to the negative electrode Fig. 2(f) reveals dark line-shaped contrasts indicating the location of the grain boundary (highlighted by arrows). For clarification throughout the remainder of this report regions of interest close to the positive and negative electrode are labeled with the applied field strength and the demarcation 'positive' or 'negative', respectively.

3.2. HAADF-STEM imaging

Fig. 3(a) and (b) show atomic resolution HAADF-STEM images recorded form the grain boundary core structures of the bicrystal annealed at 50 V/mm. Fig. 3(a) was recorded from an area close to the positive electrode, while Fig. 3(b) was captured close to the negative electrode. The grain boundary core structures on both sides of the bicrystal are periodic along the grain boundary plane. The width of the
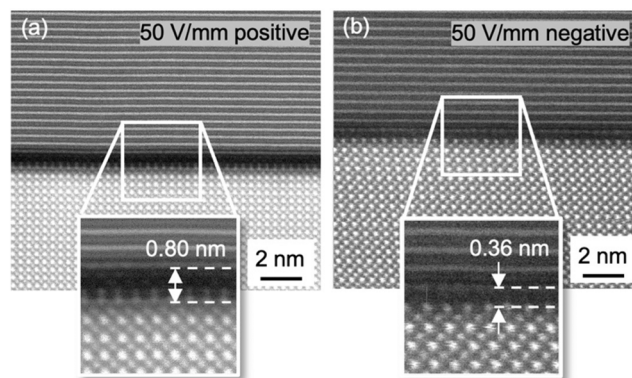

Fig. 3. HAADF-STEM images of grain boundary core structures after annealing at 50 V/mm recorded from close to (a) the positive and (b) the negative electrode.
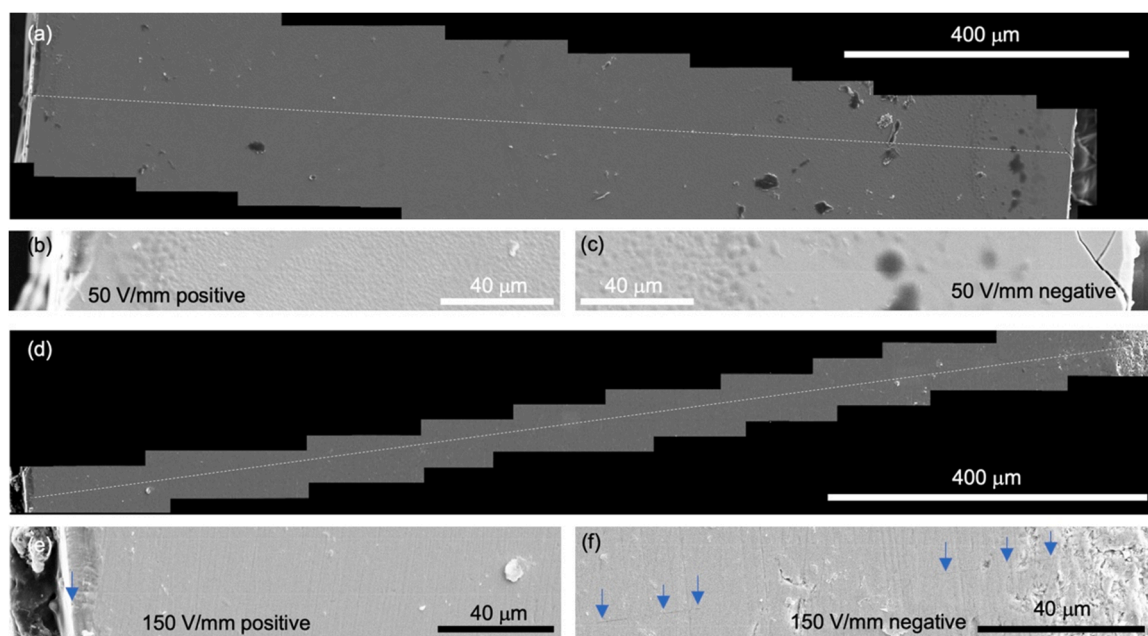

Fig. 2. (a) Assembled SE map of the grain boundary area after bicrystal annealing with a nominal field strength of 50 V/mm. The dashed line indicates the location of the grain boundary. Enlarged sections extracted from areas close to the positive (b) and negative electrodes (c) do not resolve dark intensities arising from topography due to grain boundary grooving. (d) is the SE map recorded from the bicrystal annealed while exposed to a nominal field strength of 150 V/mm. While no dark contrast identifies the location of the grain boundary plane close to the positive electrode (e), lines with dark image contrast marked by arrows identify the location of the grain boundary close to the negative electrode (f).

grain boundary core, i.e., the interface expansion, is defined as the distance between the last crystal plane in either half-crystal that is indistinguishable from the bulk. The interface expansions are approximately 0.80 nm close to the positive electrode, and only about 0.36 nm close to the negative electrode.

After electric field annealing at nominally 150 V/mm, the grain boundary expansion close to the positive electrode was roughly 0.8 nm (see Fig. 4(a)). At the negative electrode side, however, no clearly defined abrupt grain boundary core structure was observed. Instead, conventional bright field TEM imaging (Fig. 4(b) and (c)) revealed the formation of at least one secondary phase between the two adjacent half crystals. The formation of dark circles after brief exposure to the focused electron beam demonstrate that the interfacial phase is sensitive to electron beam damage. EDXS analysis of the interface structure (not shown) revealed local enrichment of $SrTiO_3$ with aluminum (Al) and silicon (Si).

3.3. Energy-loss spectroscopy

Ti $L_{2,3}$ and O K ELNES plotted in Fig. 5(a) were acquired from an area close to the negative electrode for the $SrTiO_3$ bicrystal annealed in the presence of a nominal field strength of 50 V/mm. The Ti $L_{2,3}$ ELNES line shape obtained from bulk $SrTiO_3$ exhibits well-resolved t_{2g} and e_g peak splitting of 2.4 eV for both L_2 and L_3 edges. At the grain boundary, however, the crystal field splitting is reduced to approximately 1.6 eV (cf. green spectrum in Fig. 5(a)). The O K edge in bulk $SrTiO_3$ reveals five major peaks labeled A through E. The spectrum recorded from the grain boundary plane displays a different ELNES with peaks A′, B′ and C′ that are suppressed relative to the bulk, while peak D observed in the bulk is absent at the grain boundary.

Ti $L_{2,3}$ and O K ELNES recorded form an area close to the positive electrode after annealing at 50 V/mm are plotted in Fig. 5(b). Spectra recorded from both half crystals of the bicrystal reproduce those of bulk $SrTiO_3$ (cf. Fig. 5(a)). At the grain boundary (red spectrum in Fig. 5(b)), t_{2g} and e_g peaks of the Ti $L_{2,3}$ ELNES are resolved but exhibit a slightly reduced crystal field splitting of 1.9 eV compared to 2.4 eV in bulk $SrTiO_3$. The O K ELNES recorded from the grain boundary core is less pronounced compared to the bulk but indicates otherwise almost identical line shapes.

Fig. 6 shows the Ti $L_{2,3}$ and O K ELNES recorded from an area close to the positive electrode after annealing at 150 V/mm. No EELS data was recorded from the negative electrode side of the same bicrystal due to the absence of an atomically structured grain boundary core (cf. Fig. 4 (b) & (c)). While the spectra recorded from the half crystals are indistinguishable from both those for bulk $SrTiO_3$ and those displayed in Fig. 5, the Ti $L_{2,3}$ ELNES recorded from the grain boundary core does not
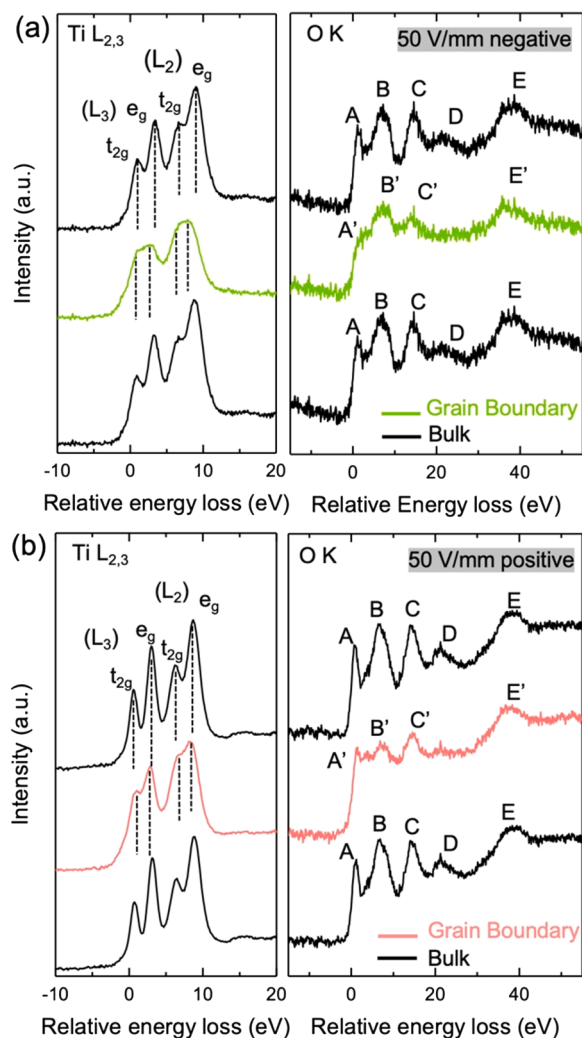

Fig. 5. Ti $L_{2,3}$ and O K edges recorded after annealing at 50 V/mm from the grain boundary core and adjacent $SrTiO_3$ half crystals close to (a) the negative and (b) the positive electrode. Spectra obtained from the $SrTiO_3$ half crystals (bulk) are all plotted in black; Ti $L_{2,3}$ and O K spectra obtained from the grain boundary are plotted in green and light red, respectively.
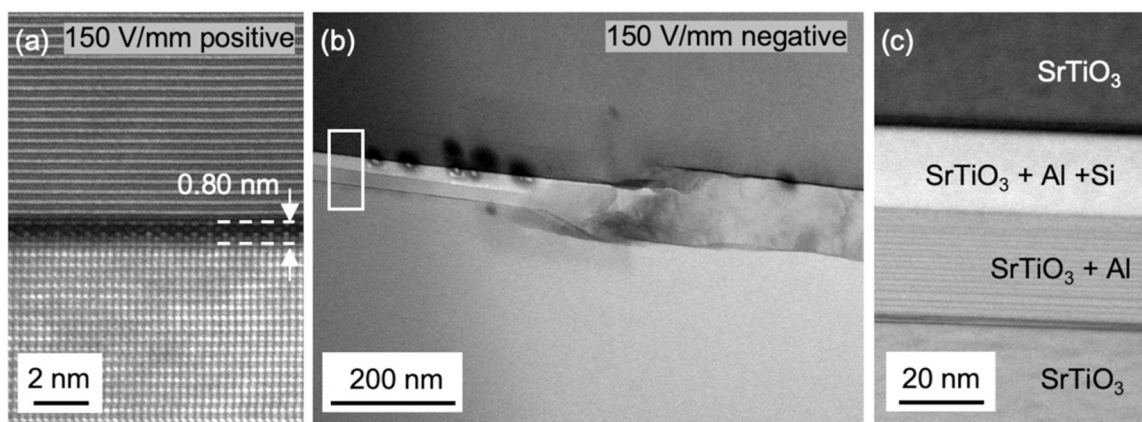

Fig. 4. (a) HAADF-STEM image of the grain boundary core recorded close to the positive electrode after field annealing at nominally 150 V/mm. (b) and (c) are bright field TEM images that were recorded close to the negative electrode and display the formation of interfacial phases. EDXS analysis (not displayed) revealed the presence of Al and/or Si.
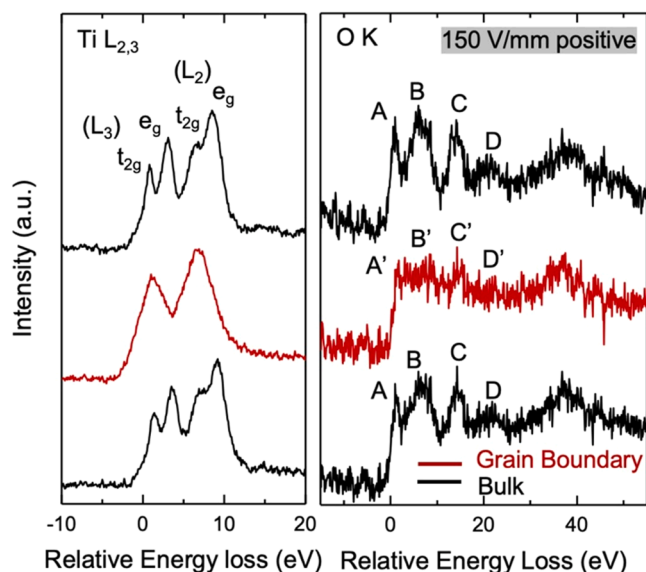
Fig. 6. Ti $L_{2,3}$ and O K edges recorded near the positive electrode after annealing at 150 V/mm from the grain boundary and adjacent SrTiO$_3$ half crystals. Spectra obtained from the SrTiO$_3$ half crystals (bulk) are all plotted in black while spectra acquired from the grain boundary are plotted in red.

present distinguishable t_{2g} and e_g signatures. The O K ELNES recorded from the grain boundary core shows a relatively small signal to noise ratio which challenges the resolution of individual ELNES peaks. However, it appears that all major peaks A through E observed for bulk SrTiO$_3$ are retained at the grain boundary core.

3.4. X-ray photoelectron spectroscopy

Fig. 7 shows XPS spectra of the Ti $2p_{3/2}$ and Ti $2p_{1/2}$ doublet acquired form a reference spectrum of single-crystalline bulk SrTiO$_3$ in comparison to data recorded from field annealed SrTiO$_3$ single crystals and surfaces of the field annealed bicrystals that included the grain boundary. All spectra in Fig. 7 were normalized with respect to the maximum intensity of the Ti(IV) peak representing an oxidation state of Ti^{4+} in bulk SrTiO$_3$ [30]. The spectra were then smoothed using Savitzky-Golay method with a quadratic polynomial [31]. Spectra recorded from the
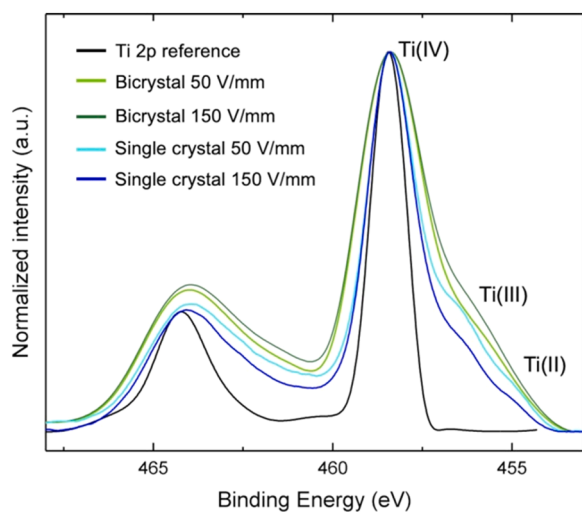

Fig. 7. Ti 2p XPS doublet for the reference single crystal (black), for bicrystals after electric field annealing at 50 V/mm (light green) and 150 V/mm (dark green), and for single crystals after annealing at 50 V/mm (light blue) and 150 V/mm (dark blue).

field-annealed samples also include spectral intensities labeled Ti(III) and Ti(II) reflecting Ti^{3+} and Ti^{2+} oxidation states, respectively [30]. After annealing in the presence of an electric field strength of nominally 50 V/mm, the spectra recorded from the bicrystal and the single crystal are indistinguishable. Annealing at 150 V/mm, however, causes the bicrystal to reveal relatively higher intensities of the Ti(III) and Ti(II) peaks, while the signals for the single crystal are smaller compared to the data recorded after annealing at 50 V/mm. The same data normalized to the total integrated intensities demonstrates that Ti(III) and Ti(II) signals increase at the cost of Ti(IV) intensities (cf. supplementary online materials).

After field annealing, the single crystals of SrTiO$_3$ were cut through their center and polished for cross-sectional XPS analysis. Ti 2p spectra were recorded from multiple equidistant locations between the surfaces that were facing the two electrodes during annealing. After peak fitting, fractional intensities of the Ti(III) and Ti(II) signatures were extracted and plotted in Fig. 8 as a function of relative distance for both field strengths. Trend lines between the data points were added to guide the eye, and the equivalent fractional intensities recorded from the surface close to the negative electrode of bicrystal samples were included for comparison. After annealing at 50 V/mm, Fig. 8(a) and (b) show that fractional intensities for Ti(III) and Ti(II) remain mostly unchanged between the two electrodes. The fractional Ti(II) intensities throughout the single crystal are in good agreement with those observed from the negative electrode side of the bicrystal. The trendline in Fig. 8(a) suggests a gradual increase of Ti(III) when approaching the negative electrode. Ti(III) intensities recorded form the single crystal, however, do not reproduce those observed from the bicrystal. After annealing at 150 V/mm, fractional intensities for Ti(III) and Ti(II) show trends with non-zero slopes between the two electrodes. Fractional intensities for Ti(III) gradually decrease when approaching the negative electrode and diverge from the data observed from the bicrystal (see Fig. 8(a)). In contrast, fractional intensities for Ti(II) increase when approaching the negative electrode and converge towards the fractional intensities observed from the bicrystal.

4. Discussion

SEM and STEM imaging of the near 45° (100) bicrystals of SrTiO$_3$ has shown that thermal annealing in the presence of an electric field directed parallel to the grain boundary plane alters grain boundary core structures. For a nominal field strength of 50 V/mm, no topography variations due to grain boundary grooving were detected by SEM (cf. Fig. 2(a)) indicating a relatively dense interface structure without extensive pore formation [32]. HAADF-STEM imaging however has revealed different interface expansions of about 0.8 nm close to the positive electrode, and only around 0.4 nm close to the negative electrode. The widths of grain boundary cores observed in this study are consistent with those previously observed from grain boundaries with almost identical misorientation angles that were diffusion bonded with electric fields directed across the interface plane [19]. The application of electric bias to (100) surfaces of SrTiO$_3$ alters the oxygen stoichiometry of the free surface depending on the polarization [33]. The resulting large oxygen concentration gradient across the interface plane during diffusion bonding was reported to be responsible for the narrowing of the grain boundary core structure in the presence of an electric field. The observed variation of the width of the grain boundary core along the interface plane indicates the migration of oxygen vacancies that was previously suggested by Rheinheimer and co-workers [17]. Local cation re-arrangement at the grain boundary occurs to accommodate charge neutrality.

It is expected that the change in grain boundary structure correlates with the distribution of the electric field along the grain boundary plane. It remains unclear whether the width of the grain boundary core, the local atomic structure, and ultimately the oxygen vacancy distribution changes gradually or abruptly along the interface plane. Modeling of the
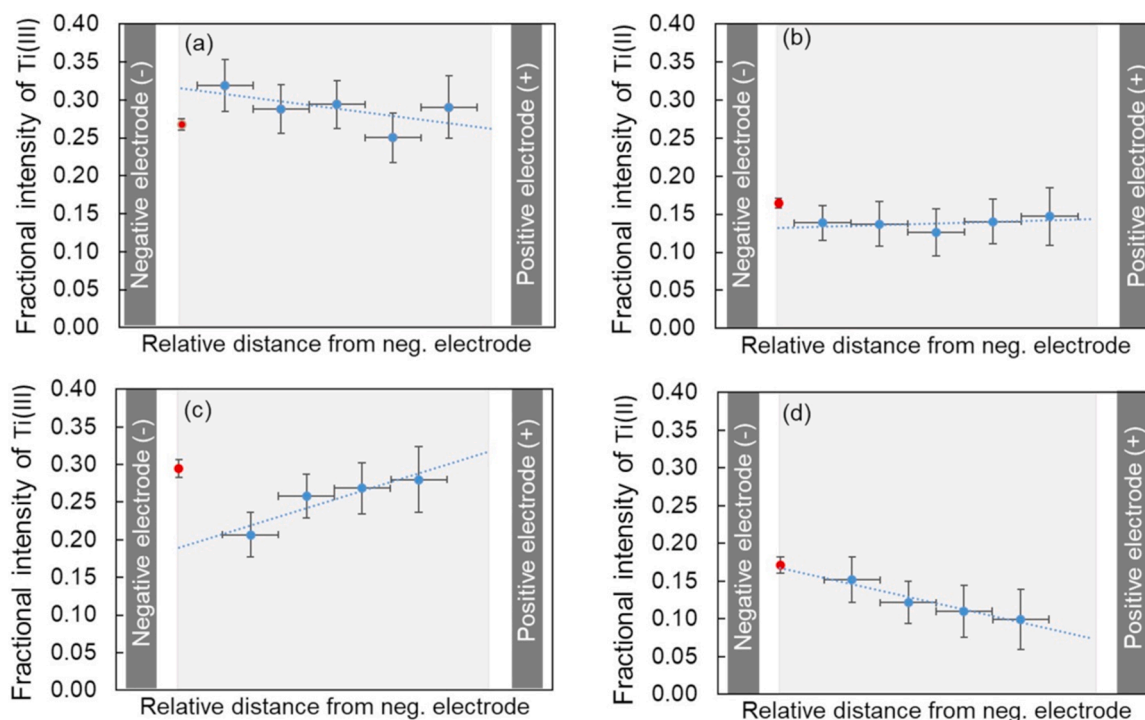
Fig. 8. Fractional intensities of the Ti(III) and Ti(II) signatures as a function of relative distance recorded after annealing at 50 V/mm (displayed in (a) and (b)) and 150 V/mm (displayed in (c) & (d)), respectively. The light grey background marks the location of the $SrTiO_3$ single crystal between the two electrodes. XPS data were acquired from equal distant locations of field-annealed single crystals of $SrTiO_3$. The red data points represent XPS measurements recorded from the surface of the $SrTiO_3$ bicrystal close the negative electrode. The dashed line is a trend line and serves as a guide to the eye.

electric field distribution and more detailed STEM characterization are required but were beyond the scope of this study.

ELNES experiments of the bicrystal annealed at 50 V/mm carried out close to the negative and positive electrodes demonstrate a reduction of Ti at the grain boundary compared to the bulk. The crystal field splitting of the t_{2g} and e_g states is smaller close to the negative electrode, indicating a stronger modification of TiO_6 octahedra that results from an increased oxygen vacancy concentration. Hughes and co-workers [19] reported a suppression of peak B in the O K ELNES line shapes for $SrTiO_3$ bicrystals bonded with no electric field indicating alterations of Sr-O bonding [34,35]. Muller also reported similar results for $SrTiO_3$ with low oxygen vacancy concentration [36]. ELNES line shapes recorded in this study from areas close to the positive electrode exhibit an only slightly dampened peak B. From this observation it is concluded that the oxygen vacancy concentration and, hence, the local space charge configuration of the bicrystal close to the positive electrode is dominated by the structural inhomogeneity caused by the misorientation of the adjacent half crystals, and is less affected by the applied electric field. In the same area, ELNES line shapes for the O K edge are similar to bulk $SrTiO_3$ with all five major peaks resolved albeit less pronounced. This observation suggests marginal re-arrangement of oxygen anions and a negligible contribution of oxygen vacancies [18]. However, the ELNES line shapes of O K edge acquired at the negative electrode side of the bicrystal differs dramatically as the two major peaks labeled A and D are mostly absent. Peak A originates from the hybridization of titanium 3d orbitals and oxygen 2p orbitals. Peak D originates from the splitting of Ti 3d orbitals that is reflected at higher electron energy losses. The absence of both peaks indicates that the Ti-O bonding close to the negative electrode is different than that at the positive side, which can be attributed to a distortion on the oxygen sublattice and local reduction of the Ti^{4+}. The O K ELNES recorded close to the negative electrode is indeed consistent with a bonding configuration in a reduced titanium oxide [37]. The combination of atomic resolution imaging and energy-loss spectroscopy confirms that, within an applied electric field,

the positively charged oxygen vacancies migrate along the grain boundary plane towards the negative electrode, hence resulting in a local enrichment of oxygen vacancies.

After annealing of the bicrystal in the presence of a nominal field strength of 150 V/mm, SEM micrographs recorded from areas close to the negative electrode reveal significant topography contrast due to grain boundary grooving. Such contrast is absent close to the positive electrode. This observation suggests considerable alterations of the grain boundary core structure both as a function of proximity of the negative electrode, and the applied electric field strength. STEM observations from the grain boundary close to the positive electrode reveal a periodic interface structure along the interface plane with a width of the grain boundary core of around 0.8 nm. This result is similar to that observed from the area close to the positive electrode after annealing at a lower nominal field strength of only 50 V/mm. Close to the negative electrode,
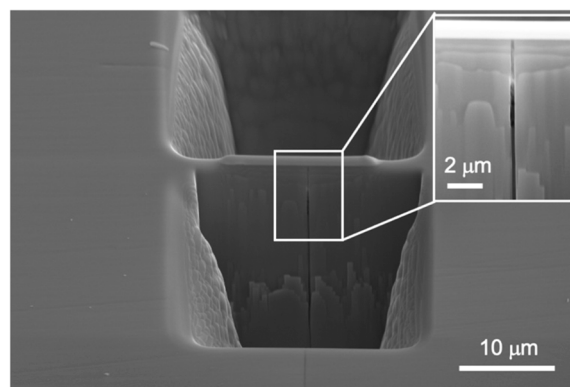

Fig. 9. SEM image of the FIB lamella recorded during TEM specimen preparation. The region of interest revealed no strong topography contrast near the 150 V/mm negative electrode. The inset shows a higher magnification cross-sectional view of the grain boundary with darker image contrast.

however, FIB lamella extracted from areas that did not show strong topography contrast (see arrow in Fig. 2b) revealed a broad dark contrast during ion-beam thinning (cf. Fig. 9).

Subsequent STEM characterization (Fig. 4(b) & (c)) revealed the formation of at least two beam-sensitive interfacial phases that are enriched with Al and Si. From this observation it is concluded that the relatively high applied field strength caused the migration of oxygen vacancies towards the negative electrode. The local enrichment of oxygen vacancies destabilizes the grain boundary which led to its decomposition observed in Fig. 4(b) and (c). Rodenbücher et al. [38] have previously shown that DC fields and the presence of oxygen vacancies can cause local reduction and induce stoichiometry polarization which allows for a controlled decomposition of $SrTiO_3$. Similar kinetic unmixing was reported for high oxygen deficiencies for $BaTiO_3$ [39] and for $NiTiO_3$ [40] which crystallizes with the ilmenite structure. The insertion of Al and Si into the highly defective grain boundary region close to the negative electrode likely resulted from insufficiently suppressed solid state diffusion from Al_2O_3 sheets during thermal annealing (cf. Fig. 1), and 0.01 wt% $SiO2$ impurities within the ZrO_2 powder. The absence of Al and Si in areas close to the positive electrode or after annealing at lower field strength indicates that the enrichment of oxygen vacancies represents an increased driving force for impurity migration for Al and Si. Studies by Bowes et al. [41] and Chan et al. [42] suggest that Si incorporates in $SrTiO_3$ as a charge neutral defect and has negligible effect on conductivity. Al serves as an acceptor and substitutes for Ti while weakly interacting with native oxygen vacancies.

XPS experiments (cf. Fig. 7) confirm the expected formation of oxygen vacancies due to the applied electric field by the appearance of Ti (III) and Ti(II) signatures that reflect Ti^{3+} and Ti^{2+} oxidation states. Neither were detected from bulk $SrTiO_3$ prior to electric field annealing. XPS spectra from the single crystal and the bicrystal recorded after field annealing at 50 V/mm are indistinguishable, which suggests that the oxygen vacancy concentrations resolved by XPS are dominated by the electric field and not by the charge compensation mechanism related to the grain boundary. However, after annealing at 150 V/mm, Ti^{3+} and Ti^{2+} intensities decrease in bulk $SrTiO_3$ compared to the smaller field strength and increase for the bicrystal. Thus, at sufficiently high field strength, the generation of oxygen vacancies may be counteracted by re-filling of vacancy sites with oxygen from the atmosphere. Additional annealing experiments under vacuum conditions would allow for additional experimental verification. This kinetic effect of oxygen re-filling, however, describes the decrease of the vacancy concentration compared to that observed at lower field strength. In the case of the bicrystal, however, comparison of Fig. 8(c) and (d)–(a) and (b), respectively, suggests that the increased field strength causes the formation of more Ti^{2+} states by further reducing Ti^{3+} close to the negative electrode, indicating a beginning electrolytic decomposition.

5. Conclusions

This study provides direct experimental evidence for oxygen vacancy redistribution along a twist grain boundary in $SrTiO_3$ when an external electric field is applied. Field annealing at a nominal field strength of 50 V/mm causes a larger grain boundary expansion near the positive electrode compared to areas close to the negative electrode. ELNES analysis of electronic grain boundary structures combined with XPS experiments confirmed the migration of oxygen vacancies towards the negative electrode during electric field annealing. For sufficiently high field strengths, oxygen vacancy agglomeration near the negative electrode can cause decomposition of the grain boundary structure. However, XPS experiments also suggest that during annealing at relatively high field strength it may become energetically more favorable to fill vacancy sites with oxygen from atmosphere. The experimental results presented in this study were obtained from a general (100) twist grain boundary in $SrTiO_3$. For general grain boundaries the interface energy varies slowly with the misorientation angle. It is therefore expected that

in the case of general grain boundaries electric fields directed along the interface plane can alter grain boundary atomic and electronic core structures by the redistribution of oxygen vacancies as a function of the externally applied field strength. In addition, anisotropy of the field effects are feasible depending on the specific grain boundary structures, especially in the case of tilt grain boundaries. It may therefore become feasible to replace variations of oxygen partial pressure atmospheres during ceramic manufacturing by the application of electric fields.

Declaration of Competing Interest

The authors declare that they have no known competing financial interests or personal relationships that could have appeared to influence the work reported in this paper.

Appendix A. Supporting information

Supplementary data associated with this article can be found in the online version at doi:10.1016/j.jeurceramsoc.2022.11.028.

References

[1] O. Guillon, R.A. De Souza, T.P. Mishra, W. Rheinheimer, Electric-field-assisted processing of ceramics: nonthermal effects and related mechanisms, MRS Bull. 46 (1) (2021) 52–58, https://doi.org/10.1557/s43577-020-00008-w.

[2] Z.A. Munir, U. Anselmi-Tamburini, M. Ohyanagi, The effect of electric field and pressure on the synthesis and consolidation of materials: a review of the spark plasma sintering method, J. Mater. Sci. 41 (3) (2006) 763–777, https://doi.org/10.1007/s10853-006-6555-2.

[3] Z.A. Munir, D.V. Quach, M. Ohyanagi, Electric current activation of sintering: a review of the pulsed electric current sintering process, J. Am. Ceram. Soc. 94 (1) (2011) 1–19, https://doi.org/10.1111/j.1551-2916.2010.04210.x.

[4] M. Yu, S. Grasso, R. Mckinnon, T. Saunders, M.J. Reece, Review of flash sintering: materials, mechanisms and modelling, Adv. Appl. Ceram. 116 (1) (2017) 24–60, https://doi.org/10.1080/17436753.2016.1251051.

[5] O. Guillon, J. Gonzalez-Julian, B. Dargatz, et al., Field-assisted sintering technology/spark plasma sintering: mechanisms, materials, and technology developments, Adv. Eng. Mater. 16 (7) (2014) 830–849, https://doi.org/10.1002/adem.201300409.

[6] H. Majidi, K. van Benthem, Consolidation of partially stabilized ZrO2 in the presence of a noncontacting electric field, Phys. Rev. Lett. 114 (19) (2015), 195503, https://doi.org/10.1103/PhysRevLett.114.195503.

[7] E.A. Olevsky, S. Kandukuri, L. Froyen, Consolidation enhancement in spark-plasma sintering: impact of high heating rates, J. Appl. Phys. 102 (11) (2007), 114913–114913.

[8] S. Schwarz, A.M. Thron, J. Rufner, K. Benthem, O. Guillon, Low temperature sintering of nanocrystalline zinc oxide: effect of heating rate achieved by field assisted sintering/spark plasma sintering, J. Am. Ceram. Soc. 95 (8) (2012) 2451–2457, https://doi.org/10.1111/j.1551-2916.2012.05205.x.

[9] R. Chaim, Densification mechanisms in spark plasma sintering of nanocrystalline ceramics, Mater. Sci. Eng. A 443 (1–2) (2007) 25–32.

[10] D. Yang, H. Conrad, Enhanced Sintering Rate and Finer Grain Size in Yttria-Stablized Zirconia (3Y-TZP) with Combined DC Electric Field and Increased Heating Rate, 2010. ⟨https://doi.org/10.1016/j.msea.2010.10.041⟩.

[11] S. Ghosh, A.H. Chokshi, P. Lee, R. Raj, A Huge Effect of Weak dc Electrical Fields on Grain Growth in Zirconia, 92(8), 2009, pp. 1856–1859. ⟨https://doi.org/10.1111/j.1551–2916.2009.03102.x⟩.

[12] J.F. Rufner, D. Kaseman, R.H.R. Castro, K. van Benthem, DC electric field-enhanced grain-boundary mobility in magnesium aluminate during annealing, J. Am. Ceram. Soc. 99 (6) (2016) 1951–1959, https://doi.org/10.1111/jace.14157.

[13] W. Rheinheimer, M. Fülling, M.J. Hoffmann, Grain growth in weak electric fields in strontium titanate: grain growth acceleration by defect redistribution, J. Eur. Ceram. Soc. 36 (11) (2016) 2773–2780, https://doi.org/10.1016/j.jeurceramsoc.2016.04.033.

[14] W. Qin, H. Majidi, J. Yun, K. van Benthem, Electrode effects on microstructure formation during FLASH sintering of yttrium-stabilized zirconia, J. Am. Ceram. Soc. 99 (7) (2016) 2253–2259, https://doi.org/10.1111/jace.14234.

[15] J.-W. Jeong, J.-H. Han, D.-Y. Kim, Effect of electric field on the migration of grain boundaries in alumina, J. Am. Ceram. Soc. 83 (4) (2000) 915–918, https://doi.org/10.1111/j.1151-2916.2000.tb01294.x.

[16] T.P. Mishra, R.R.I. Neto, G. Speranza, et al., Electronic conductivity in gadolinium doped ceria under direct current as a trigger for flash sintering, Scr. Mater. 179 (2020) 55–60, https://doi.org/10.1016/j.scriptamat.2020.01.007.

[17] W. Rheinheimer, J.P. Parras, J.-H. Preusker, R.A. De Souza, M.J. Hoffmann, Grain growth in strontium titanate in electric fields: The impact of space-charge on the grain-boundary mobility, J. Am. Ceram. Soc. 102 (6) (2019) 3779–3790, https://doi.org/10.1111/jace.16217.

[18] L.A. Hughes, M. Marple, K. van Benthem, Electrostatic fields control grain boundary structure in SrTiO3, Appl. Phys. Lett. 113 (4) (2018) 041604, https://doi.org/10.1063/1.5039646.

[19] L.A. Hughes, K. van Benthem, Effects of electrostatic field strength on grain-boundary core structures in SrTiO3, J. Am. Ceram. Soc. 102 (8) (2019) 4502–4510, https://doi.org/10.1111/jace.16344.

[20] M. Nishi, T. Tanaka, K. Matsunaga, Y. Ikuhara, T. Yamamoto, Non-linear Current-Voltage Property across Æ5(210) Symmetric Tilt Boundary in Nb-Doped SrTiO3 Bicrystal. n.d.;5.

[21] S. Hutt, O. Kienzle, F. Ernst, M. Rühle, Processing and structure of grain boundaries in strontium titanate, Z. fur Metallkd. 92 (2) (2001) 105–109.

[22] O.M. Akselsen, Diffusion bonding of ceramics, J. Mater. Sci. 27 (3) (1992) 569–579, https://doi.org/10.1007/BF00554019.

[23] A. Hill, E. Wallach, Modelling of Solid-State Diffusion Bonding. n.d. ⟨https://doi.org/10.1016/0001–6160(89)90040-0⟩.

[24] W.H. Rhodes, W.D. Kingery, Dislocation dependence of cationic diffusion in SrTiO3, J. Am. Ceram. Soc. 49 (10) (1966) 521–526, https://doi.org/10.1111/j.1151-2916.1966.tb13155.x.

[25] L.A. Hughes, K. van Benthem, Formation of SrTiO3 bicrystals using spark plasma sintering techniques, Scr. Mater. 118 (2016) 9–12, https://doi.org/10.1016/j.scriptamat.2016.03.005.

[26] L.A. Hughes, K. van Benthem, Spark plasma sintering apparatus used for the formation of strontium titanate bicrystals, J. Vis. Exp. 120 (2017), https://doi.org/10.3791/55223 (e55223–55223).

[27] R.F. Egerton, An introduction to EELS, in: R.F. Egerton (Ed.), Electron Energy-Loss Spectroscopy in the Electron Microscope, Springer US, Boston, MA, 2011, pp. 1–28, https://doi.org/10.1007/978-1-4419-9583-4_1.

[28] F. Peña, E. de la, Prestat, V.T. Fauske , et al. hyperspy/hyperspy: Release v1.6.5. Zenodo, 2021. ⟨https://doi.org/10.5281/zenodo.5608741⟩.

[29] P. Oelhafen, in: D. Briggs, M.P. Seah (Eds.), Practical Surface Analysis by Auger and X-ray Photoelectron Spectroscopy, John Wiley and Sons, 1983, p. 533. ISBN 0471 26279 X. Elsevier; 1984.

[30] C. Powell, X-ray Photoelectron Spectroscopy Database XPS,Version 4.1, NIST Standard Reference Database 20, 1989. ⟨https://doi.org/10.18434/T4T88K⟩.

[31] P.A. Gorry, General least-squares smoothing and differentiation by the convolution (Savitzky-Golay) method, Anal. Chem. 62 (6) (1990) 570–573, https://doi.org/10.1021/ac00205a007.

[32] L.A. Hughes, K. van Benthem, Low angle twist boundary in SrTiO3 fabricated by spark plasma sintering techniques, J. Am. Ceram. Soc. (2018), https://doi.org/10.1111/jace.15863.

[33] T. Leisegang, H. Stöcker, A.A. Levin, et al., Switching Ti Valence in ${\mathrm{SrTiO}}_{3}$ by a dc electric field, Phys. Rev. Lett. 102 (8) (2009), 087601, https://doi.org/10.1103/PhysRevLett.102.087601.

[34] H. Seo, A.B. Posadas, C. Mitra, A.V. Kvit, J. Ramdani, A.A. Demkov, Band alignment and electronic structure of the anatase TiO$_{2}$/SrTiO$_{3}$(001) heterostructure integrated on Si(001), Phys. Rev. B 86 (7) (2012), 075301, https://doi.org/10.1103/PhysRevB.86.075301.

[35] J. Zhang, Application of electron energy-loss spectroscopy to ferroelectric thin films, Halle (Saale), Univ., Diss. (2004) 2004.

[36] D.A. Muller, N. Nakagawa, A. Ohtomo, J.L. Grazul, H.Y. Hwang, Atomic-scale imaging of nanoengineered oxygen vacancy profiles in SrTiO3, Nature 430 (7000) (2004) 657–661, https://doi.org/10.1038/nature02756.

[37] C.-N. Huang, J.-S. Bow, Y. Zheng, S.-Y. Chen, N. Ho, P. Shen, Nonstoichiometric titanium oxides via pulsed laser ablation in water, Nanoscale Res Lett. 5 (6) (2010) 972–985, https://doi.org/10.1007/s11671-010-9591-4.

[38] C. Rodenbücher, P. Meuffels, G. Bihlmayer, et al., Electrically controlled transformation of memristive titanates into mesoporous titanium oxides via incongruent sublimation, Sci. Rep. 8 (1) (2018) 3774, https://doi.org/10.1038/s41598-018-22238-4.

[39] H.-I. Yoo, C.-E. Lee, R.A. De Souza, M. Martin, Equal mobility of constituent cations in BaTiO3, Appl. Phys. Lett. 92 (25) (2008), 252103.

[40] J. Chun, M. Martin, H.-I. Yoo, Electrotransport-induced unmixing and decomposition of ternary oxides, J. Appl. Phys. 117 (12) (2015), 124504, https://doi.org/10.1063/1.4915626.

[41] P.C. Bowes, J.N. Baker, J.S. Harris, B.D. Behrhorst, D.L. Irving, Influence of impurities on the high temperature conductivity of SrTiO$_3$, Appl. Phys. Lett. 112 (2) (2018), 022902, https://doi.org/10.1063/1.5000363.

[42] N. -H. Chan, R.K. Sharma, D.M. Smyth, Nonstoichiometry in SrTiO3, J. Electrochem Soc. 128 (8) (1981) 1762–1769, https://doi.org/10.1149/1.2127727.